

## Merged-Element Transmons: Design and Qubit Performance

H.J. Mamin<sup>1,\*</sup>, E. Huang,<sup>1,†</sup> S. Carnevale,<sup>2</sup> C.T. Rettner,<sup>1</sup> N. Arellano,<sup>1</sup> M.H. Sherwood,<sup>1</sup> C. Kurter,<sup>2</sup> B. Trimm<sup>2</sup>, M. Sandberg<sup>1,‡</sup>, R.M. Shelby,<sup>1</sup> M.A. Mueed,<sup>1</sup> B.A. Madon,<sup>1</sup> A. Pushp,<sup>1</sup> M. Steffen<sup>1,‡</sup>, and D. Rugar<sup>1,‡</sup>

<sup>1</sup>IBM Quantum, IBM Almaden Research Center, San Jose, California 95120, USA

<sup>2</sup>IBM Quantum, IBM T. J. Watson Research Center, Yorktown Heights, New York 10598, USA



(Received 16 March 2021; revised 27 May 2021; accepted 14 July 2021; published 13 August 2021)

We demonstrate a superconducting transmon qubit in which a Josephson junction has been engineered to act as its own parallel shunt capacitor. This merged-element transmon potentially offers a smaller footprint than conventional transmons. Because it concentrates the electromagnetic energy inside the junction, it reduces the relative electric field participation from other interfaces. By combining micrometer-scale Al/AIO<sub>x</sub>/Al junctions with long oxidations, we produce functional devices with  $E_J/E_C$  in the low-transmon regime ( $E_J/E_C \lesssim 30$ ). Cryogenic  $I$ - $V$  measurements show a sharp  $dI/dV$  structure with low subgap conduction. Qubit spectroscopy of tunable versions shows a small number of avoided level crossings, suggesting the presence of two-level systems. We observe mean  $T_1$  times typically in the range of 10–90  $\mu$ s, with some annealed devices exhibiting  $T_1 > 100 \mu$ s over several hours. The results suggest that energy relaxation in conventional small-junction transmons is not limited by junction loss.

DOI: 10.1103/PhysRevApplied.16.024023

### I. INTRODUCTION

The superconducting transmon qubit [1] has become a workhorse in the field of quantum computation and is the fundamental building block in some of the most sophisticated quantum computation systems built to date [2,3]. The transmon consists of a Josephson junction (JJ) in parallel with a coplanar shunt capacitor, forming a simple nonlinear  $LC$  circuit. The shunt capacitor acts to exponentially suppress charge noise while retaining enough anharmonicity to allow individual quantized transitions to be addressed. In principle, it could be made simpler by engineering the junction self-capacitance to be large enough to act as its own shunt capacitor, eliminating the need for an external capacitor [4,5]. Such qubits could also be significantly more compact, allowing for a higher areal density of qubits. Moreover, because they concentrate the energy inside the junction, the relative importance of other lossy interfaces and surfaces should be reduced. This could conceivably lead to improved coherence if high quality (e.g., epitaxial) dielectrics can be developed [4,6,7]. This concept has been dubbed the merged-element transmon, or MET [5].

### II. DESIGN AND SIMULATION

The tunnel junction at the heart of the MET does double duty as a Josephson element and a parallel-plate capacitor. The dimensions are constrained by the target capacitance as well as the thickness and dielectric constant of the insulating tunnel barrier. The exact dielectric thickness is not known *a priori* but must be in a limited range, given the exponential dependence of the critical current on the thickness. Accordingly, as a starting point, we assume an oxide thickness of 2 nm with a dielectric constant of 10, appropriate for the Al/AIO<sub>x</sub>/Al tunnel junctions that we use for these initial studies. Applying the formula for a simple parallel-plate capacitor gives a junction area of roughly 1.4  $\mu\text{m}^2$  to achieve a junction capacitance of 62 fF. In principle, since the junction area and the qubit area could be one and the same, the qubit footprint could be greatly reduced compared to conventional transmons that use coplanar capacitors with dimensions of hundreds of micrometers [8]. In terms of junction dimensions, the MET falls somewhere between a transmon, with submicron junction dimensions, and phase qubits, which are self-shunting like the MET but are typically much larger laterally and capacitively, increasing the probability of being plagued by two-level systems (TLSs) [9,10].

The MET geometry results in two significant challenges related to the fact that the MET lateral dimensions are large for a junction but small for a capacitor. On the one hand, the small capacitor geometry gives very little area

\*mamin@us.ibm.com

†ehuang@us.ibm.com

‡rugar@us.ibm.com

for capacitive coupling to the drive and readout circuitry. On the other hand, the junction area is up to 2 orders of magnitude larger than for typical transmon junctions. To achieve the same critical current needed for 4–5 GHz qubit operation (typically about 24 nA) therefore requires making the tunnel barrier appropriately thicker.

Assuming that a junction of proper capacitance can be made, the chief design decision becomes how to couple to it. For the present work, we choose to use coplanar capacitive coupling to the readout and drive resonator for simplicity, with a target coupling strength  $g/2\pi$  of at least 20 MHz to obtain an adequate readout signal-to-noise ratio. An additional constraint is that the coplanar coupling structure should not add substantially to the overall capacitance, so as not to detract unduly from the self-shunting nature of the junction. Using finite-element simulations (ANSYS Q3D) to guide the design, we satisfy the constraints using the geometry shown in Figs. 1(a) and 1(b). Two 100- $\mu\text{m}$ -long arms with widths of 0.5  $\mu\text{m}$  extend out perpendicularly from the junction region; these arms act as antennas and allow for coupling to a readout resonator and ground plane, respectively. The coplanar contribution from just the arms to the overall capacitance, calculated by removing the

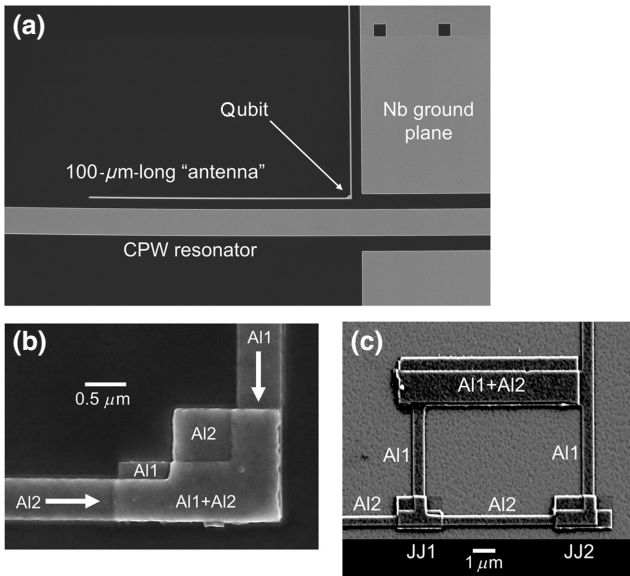


FIG. 1. Scanning electron micrographs of MET devices. (a) The MET consists of a micrometer-size tunnel junction capacitively coupled to a coplanar waveguide resonator via 100- $\mu\text{m}$ -long, 0.5- $\mu\text{m}$ -wide “antenna” structures. The resonator, which serves to both excite the qubit and read out its state, has a resonant frequency around 7 GHz. (b) An enlargement of the junction region. The various levels and shapes are a consequence of the angled evaporation and shadowing by the resist layer. The azimuthal directions of the two evaporation are indicated by arrows. The junction area is determined by the overlap of Al1 and Al2, which in this case is approximately  $1.4 \mu\text{m}^2$ . (c) A two-junction device that serves as a flux-tunable qubit.

TABLE I. A comparison of typical qubit properties. The MET entries are initial targeted values. The properties for conventional transmons represent calculated and inferred values for typical geometries as given in the references.

Property	MET	Conventional transmon [8,11,12]
Junction area ( $\mu\text{m}^2$ )	1.4	0.01–0.03
Junction capacitance, $C_{\text{JJ}}$ (fF)	62	0.5–1.3
Total capacitance, $C_{\text{total}}$ (fF)	67	60
Junction participation, $p_{\text{JJ}}$	0.93	0.008–0.02
Substrate-vacuum participation ( $\text{nm}^{-1}$ )	$3.5 \times 10^{-5}$	$5.0 \times 10^{-5}$

overlapping junction region, is 5.0 fF. Thus, with a junction capacitance of approximately 62 fF, the junction is responsible for 93% of the overall device capacitance (Table I). In future designs, the 7% contribution from the arms could be made even less by extending the arms out at a  $180^\circ$  instead of  $90^\circ$  angle. While our geometry gives up a substantial amount of the areal-density advantage of the MET, with the junction itself representing only a small fraction of the device footprint, it is still considerably smaller than many other transmon designs [8,13].

This approach successfully solves the coupling problem, with the coupling factor  $g/2\pi$  predicted to be roughly 27 MHz for the antennas spaced at 4  $\mu\text{m}$  from the readout resonator and ground plane. The coupling could in principle be made more compact by decreasing the spacing of the antenna arms from the resonator and ground or by creating interdigitated structures. However, finite-element simulations show that significant substrate-vacuum participation is associated with the coupling regions, where high electric fields exist. Compared to a typical conventional transmon with a coplanar shunt capacitor, such as the “mod D” design in Ref. [8], the substrate-vacuum participation is calculated to be reduced only by roughly 30%, setting an upper limit on the coherence gains that might be observed if the substrate-vacuum interface is particularly lossy. Going to a parallel-plate-type coupler [5], though not as simple to fabricate, might allow for higher coupling with a reduced surface participation and footprint.

### III. FABRICATION

For MET fabrication, we aim for a total capacitance of 67 fF and a critical current of 24 nA to produce qubits with a frequency around 5 GHz, an anharmonicity of 350 MHz, and an  $E_J/E_C$  ratio near 40 [1]. As the optimal junction area and oxidation conditions are not known initially, devices with various junction areas and oxidations are fabricated to explore the electrical characteristics and qubit performance.

All devices are fabricated on intrinsic high-resistivity (100) silicon wafers. Prior to junction fabrication, niobium structures (e.g., coplanar waveguide resonators) are fabricated using a standard optical-lithography process ( $\lambda = 248$  nm), followed by reactive ion etching.

Junctions with areas ranging from 1 to  $2.4 \mu\text{m}^2$  are fabricated using a variation of a bridgeless “Manhattan” approach [14–17]. In this approach, an electron-beam lithography pattern is defined in a 660-nm-thick positive-tone bilayer resist, with narrow regions defining the antenna arms and a larger overlap region where the junction is to be formed. An initial 50-nm-thick aluminum deposition (Al1) is performed at a  $45^\circ$  incident polar angle, with the azimuthal direction aligned along the direction of one of the antenna arms having a width of 500 nm [Fig. 1(b)]. This Al1 deposition thus forms one arm as well as the base electrode of the junction. No aluminum is deposited along the perpendicular arm due to the narrowness of the antenna pattern and the shadowing effect of the resist stack.

The sample is then moved to a separate chamber without breaking vacuum for oxidation in order to form the tunnel barrier. To achieve the desired junction critical current, a relatively thick tunnel barrier is needed, which requires rather long oxidations at relatively high oxygen pressure. Typical values are 1–4 h at 600 torr of  $\text{O}_2$  (more details below).

After oxidation, the wafer is rotated by an azimuthal angle of  $90^\circ$  for the second deposition. This deposition of aluminum (Al2) is 100 nm thick and forms both the counter electrode and the second antenna arm. Subsequently, the devices are exposed to a solvent strip to remove the bilayer resist and lift off the Al1/Al2 layers residing atop the resist. The resulting structure is shown in Fig. 1(b), where the overlap region of the two depositions forms the tunnel junction.

In addition to single-junction devices, we also fabricate a two-junction version of the MET in order to have a flux-tunable device. The finished device, shown in Fig. 1(c), has two equal-area Josephson junctions connected in parallel to form a superconducting quantum interference device (SQUID) loop configuration. Due to the fabrication process, this two-junction device has a parasitic junction, seen as the larger rectangle at the top of the micrograph, where there is an overlap of the base and counter electrode layers.

Since MET performance is dominated by the quality of the tunnel junction, a number of oxidation conditions and heat treatments are considered in order to optimize and tune the tunnel-junction characteristics. Based on experience with conventional transmons, we initially seek room-temperature junction resistances in the neighborhood of  $10 \text{ k}\Omega$  in order to achieve Josephson critical currents around  $24 \text{ nA}$ . Using devices with a  $2.4-\mu\text{m}^2$  junction area, an initial test with a 1-h oxidation at 600 torr results in resistance values that are below our target, in the vicinity of

$5.3 \text{ k}\Omega$ . Previous studies have shown that heat treatments in the range of  $350$ – $450^\circ\text{C}$  can increase the junction resistance and improve junction quality [18–21]. Accordingly, we test the effect of rapid thermal anneal in a nitrogen atmosphere. Anneals for 5 min at both  $375$ – $425^\circ\text{C}$  are found to increase the room-temperature resistance to approximately  $6.2 \text{ k}\Omega$ .

To confirm that the fabrication process produces high quality tunnel junctions, dc current-voltage characteristics are measured at millikelvin temperature [22]. Both annealed and unannealed devices exhibit low subgap conduction and sharp turn-on at the superconducting gap, as demonstrated by the  $I$ - $V$  and  $dI/dV$  curves shown in Fig. 2. For devices subjected to the  $425^\circ\text{C}$  anneal [blue curve in Fig. 2(b)], a small increase in the superconducting gap is evident compared to the unannealed device. Gap values of  $200 \mu\text{eV}$  and  $191 \mu\text{eV}$  are found for the annealed and unannealed devices, respectively, as determined by fitting the peaks in the differential conductance to the BCS model [23]. Somewhat lower subgap conductivity is also

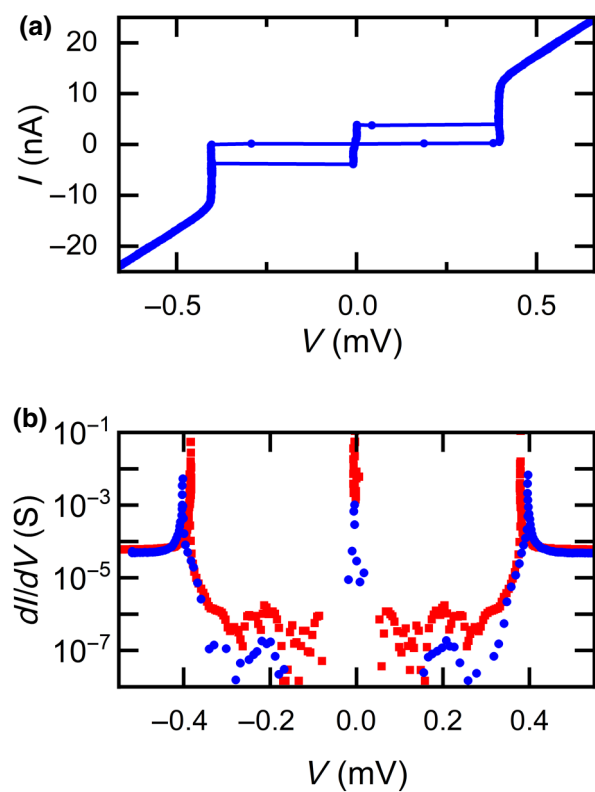


FIG. 2. The electrical characteristics of tunnel junctions with a  $1-\mu\text{m}^2$  junction area taken at  $20 \text{ mK}$ . The junction oxidation is 1 h at 600 torr. (a) The dc current-voltage characteristics. (b) The  $dI/dV$  measurement of junctions showing low subgap conductivity. The noisy data at the lowest conductance levels are limited by instrumental resolution. The blue data points are for a device annealed at  $425^\circ\text{C}$  for 5 min. It exhibits a slightly larger energy gap compared to the unannealed device (red data).

observed for the annealed junction, indicative of improved junction quality [24].

For the qubit results presented below, the oxidation time is increased to 4 h at 600 torr in order to further increase the tunneling resistance. The resulting room-temperature resistances are approximately  $6.6\text{ k}\Omega$  for unannealed junctions and  $9.0\text{ k}\Omega$  for junctions annealed at  $425^\circ\text{C}$ . For the unannealed devices, a brief argon-ion milling step is performed just prior to the deposition of Al1. This is found to improve the yield of the unannealed qubits.

#### IV. QUBIT CHARACTERIZATION

Single-junction MET qubits with junction areas of  $1.4$  and  $1.9\text{ }\mu\text{m}^2$  are characterized in a well-shielded dilution refrigerator operating below  $20\text{ mK}$  [25]. The qubits are capacitively coupled to quarter-wave coplanar waveguide resonators, which are, in turn, inductively coupled to a  $50\text{-ohm}$  feed line for transmission-mode dispersive readout. Typical resonator frequencies are around  $7\text{ GHz}$ . Functionality is evaluated using both continuous-wave (cw) and pulsed microwave excitation for unannealed and annealed devices. Table II summarizes the results for the five best-performing devices of each type.

Two-tone cw spectroscopy measurements using a vector network analyzer are used to determine the  $f_{01}$  qubit frequency as well as the anharmonicity  $\alpha/2\pi = f_{01} - f_{12} = 2f_{01} - f_{02}$  [5]. The qubit frequencies are typically in the range  $4.4\text{--}5.0\text{ GHz}$  for the unannealed devices and  $3.3\text{--}3.8\text{ GHz}$  for the annealed devices. The lower frequencies for the annealed devices are due to the lower critical current and larger Josephson inductance of the heat-treated junctions. The anharmonicities typically range from  $300$  to  $450\text{ MHz}$ . From these measurements, we can calculate  $E_J/E_C$ , the ratio of the Josephson energy to the charging energy [1]. The devices with the larger junction area ( $1.9\text{ }\mu\text{m}^2$ ) have somewhat smaller anharmonicities and larger  $E_J/E_C$  ratios, as expected from their higher capacitance. Overall, the  $E_J/E_C$  ratios are mostly in the range of  $20\text{--}30$ , which is

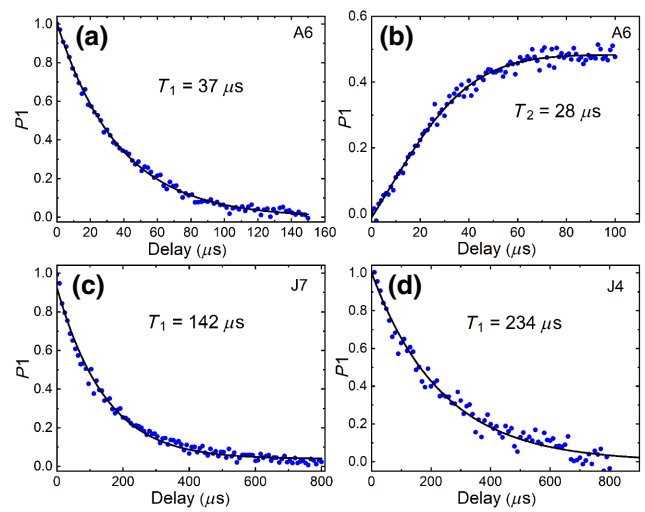


FIG. 3. Examples of measured  $T_1$  and  $T_2$ -echo decay curves plotted as the excited-state probability  $P_1$  versus the readout delay time: (a),(b) for unannealed qubit A6; (c),(d) for annealed qubits J7 and J4, respectively. Solid lines are exponential fits, except for (b), where a stretched exponential of the form  $A + B \exp[-(t/T_2)^n]$  is used, with  $n = 1.37$ .

somewhat lower than targeted. Presumably, this low ratio is responsible for the significant charge noise observed in some of the qubits.

Using pulsed time-domain sequences, we successfully measure both the energy-relaxation time  $T_1$  and the echo-decoherence time  $T_2$  for a number of qubits [26]. Figure 3 and Table II show results obtained for some of the better-performing devices. The best-performing unannealed device has a mean  $T_1$  of  $34.4\text{ }\mu\text{s}$  when averaged over several hours with 87 separate measurements. Overall, the median  $T_1$  for the 14 unannealed devices that we measure is  $13\text{ }\mu\text{s}$ , with a median qubit quality factor  $Q = 2\pi f_{01} T_1$  of  $3.8 \times 10^5$ .

The annealed devices perform considerably better. The median  $T_1$  for the eight annealed devices that we measure

TABLE II. Characteristics of selected qubits.

Qubit ID	JJ Area ( $\mu\text{m}^2$ )	$f_{01}$ (GHz)	$\alpha/2\pi$ (MHz)	$E_J/E_C$	$T_1$ ( $\mu\text{s}$ )			$T_2$ -echo ( $\mu\text{s}$ )			Mean $Q$ (M)	Type
					Best	Mean	Std. dev.	Best	Mean	Std. dev.		
J4	1.4	3.808	414	21	234	89.9	75.9	...	...	...	2.2	Annealed
K7	1.9	3.747	343	27	109	88.1	12.6	50	41.1	3.8	2.1	
J7	1.9	3.748	362	25	154	87.4	52.5	...	...	...	2.1	
K5	1.9	3.771	339	27	65	50.3	8.7	39	33.4	3.1	1.2	
J6	1.9	3.758	368	24	41	38.1	1.6	46	43.3	2.2	0.90	
A6	1.9	4.978	404	32	41	34.4	3.9	28	21.1	2.0	1.1	Unannealed
B9	1.4	4.521	439	25	23	16.9	6.4	...	...	...	0.48	
A9	1.4	4.610	426	26	29	16.1	8.6	...	...	...	0.47	
A5	1.9	5.032	417	31	32	14.6	6.2	32	20.5	6.8	0.46	
B7	1.9	4.503	376	30	15	11.8	2.3	...	...	...	0.33	

is  $46 \mu\text{s}$ , with a median  $Q$  of  $1.1 \times 10^6$ . Three of the best-performing annealed devices have mean  $T_1$  greater than  $87 \mu\text{s}$ , corresponding to quality factors above 2 million. Remarkably, one annealed qubit maintains a mean  $T_1$  greater than  $200 \mu\text{s}$  [Fig. 3(d)] over a period of several hours, before abruptly dropping down to more typical values. Similar  $T_1$  fluctuations have been seen previously in conventional transmon qubits and are believed to be due to TLSs coming into resonance with the qubit [27].

## V. QUBIT SPECTROSCOPY

Because roughly 90% of the electromagnetic energy is confined to the junction, the MET is an ideal test bed for studying the properties of the dielectric layer and losses in the junction. One approach is to perform qubit spectroscopy to look for signs of individual TLSs. This is most readily done with our flux-tunable two-junction MET [Fig. 1(c)]. A small coil electromagnet is attached to the qubit board to tune the qubit frequency. This allows for two-dimensional qubit spectroscopy, where both the coil current (magnetic flux) and the qubit pump frequency are varied. The resulting false-color plot for an annealed device is shown in Fig. 4. Two prominent avoided crossings are seen, with splittings of 20–30 MHz, similar to what has been seen in phase qubits [10,28,29].

We observe avoided crossings in both annealed and unannealed devices. In general, the avoided crossings are rare over the measured frequency range of approximately 1 GHz, but because the scans are rather coarse, it is possible that some number of smaller splittings go undetected. Nonetheless, we can naively use these measurements to obtain an order-of-magnitude estimate of

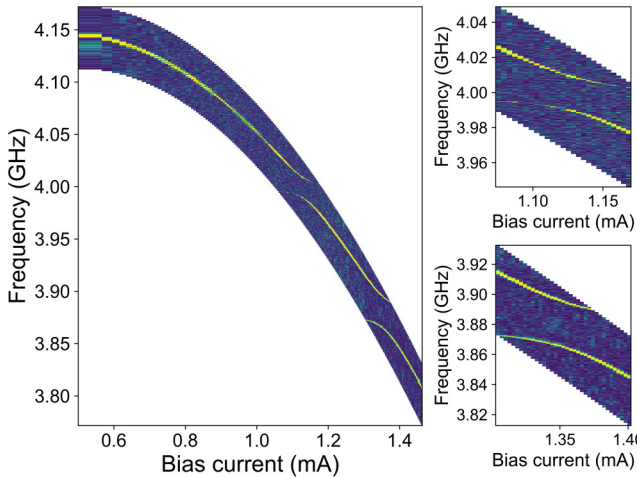


FIG. 4. Qubit spectroscopy, showing the qubit frequency as a function of the magnet bias current in a flux-tunable MET device. The detail on the right shows two prominent avoided crossings with frequency splittings on the order of 20 MHz, suggesting the presence of TLSs within the MET junction.

the density of strongly coupled TLSs in our junctions (e.g., coupling strength  $> 10 \text{ MHz}$ ). Combining results from both annealed and unannealed devices, we detect a total of 17 avoided crossings over six qubits, giving an average density of  $1.0 \mu\text{m}^{-2} \text{ GHz}^{-1}$  [30]. This value is in reasonable agreement with the value of approximately  $0.5 \mu\text{m}^{-2} \text{ GHz}^{-1}$  from Martinis *et al.*, derived from measurements on larger junctions, as well as values from other bulk and thin-film dielectrics [10,31]. Further studies will be needed to determine if there is a statistically significant difference between annealed and unannealed devices. Ultimately, reducing the TLS density will require more perfect tunnel barriers, such as those made through epitaxial means.

## VI. IMPLICATIONS FOR CONVENTIONAL SMALL-JUNCTION TRANSMONS

Given that the performance of the MET will be dominated by the loss in the junction, what does the MET tell us about junction loss in general and can this knowledge be used to make inferences about conventional small-junction transmons? Using scaling arguments and some simplifying assumptions, one can in fact argue that the junction must not be the dominant source of energy loss in conventional small-junction transmons.

We start by writing the total loss  $\Gamma_Q$  as the sum of individual loss terms [32]:

$$\Gamma_Q = p_{\text{JJ}} \tan \delta_{\text{JJ}} + \sum_i p_i \tan \delta_i, \quad (1)$$

where  $p_{\text{JJ}}$  is the fraction of the electric field energy associated with the Josephson junction,  $p_i$  represents the fraction of energy in various other materials and interfaces, and  $\tan \delta_i$  is the associated loss tangent.

The energy in the junction is just  $\frac{1}{2} C_{\text{JJ}} V^2$ , while the total energy is  $\frac{1}{2} C_{\text{total}} V^2$ . Thus  $p_{\text{JJ}} = C_{\text{JJ}}/C_{\text{total}}$ . For the MET, virtually all the capacitance is due to the junction, i.e.,  $p_{\text{JJ}} \sim 0.93$ . A conventional small-junction transmon will have much smaller capacitance and junction participation based on its smaller area. A transmon with a junction area of  $0.03 \mu\text{m}^2$ , for example [12], would be expected to have  $p_{\text{JJ}}$  about 46 times smaller than for the  $1.4 \mu\text{m}^2$  MET. Here, we make the simplifying assumption that both types of junction have roughly the same oxide thickness and loss tangent. (We note, however, that this assumption may not be valid, since the oxidation conditions are different.) Equation (1) therefore implies that the junction-loss term for this device should be 46 times smaller than for the MET. Based on the best mean  $T_1$  from Table II of  $89.9 \mu\text{s}$ , the limit on  $T_1$  imposed by the junction in a conventional transmon would then be  $4.1 \text{ ms}$ , assuming only junction loss. To the extent that such long relaxation times are not observed in conventional transmons, sources

of loss other than the junction must be limiting the coherence. This result is consistent with the conclusion reached by Wang *et al.* [32] based on a study of qubit relaxation as a function of the electric field surface participation.

Alternatively, we can use our MET results to determine an upper bound to the loss tangent of the  $\text{AlO}_x$  in the junction. We see from Eq. (1) that

$$\tan \delta_{JJ} < \Gamma_Q / p_{JJ}. \quad (2)$$

Since  $\Gamma_Q = 1/Q$ , where  $Q$  is the qubit quality factor, and  $p_{JJ} \sim 0.93$ , this implies that  $\delta_{JJ} \lesssim 1/0.93Q$ . With a best measured mean  $Q$  of  $2.2 \times 10^6$ , we find that  $\delta_{JJ} \lesssim 5 \times 10^{-7}$ .

While this loss tangent is small compared to typical literature values for  $\text{AlO}_x$ , where loss tangents on the order of  $10^{-3}$  are commonly found [10,33,34], larger values would not be compatible with the measured values of  $T_1$  for the MET. This result is also consistent with the limit of  $4 \times 10^{-8}$  obtained by Kim *et al.* through a similar argument [35]. Note that our small value for the loss tangent should be considered as an effective value in the single-photon limit and is valid only for frequencies unaffected by strongly coupled TLS resonances. The small volume of the tunnel junction is undoubtedly a key factor in avoiding problematic TLS interactions that are otherwise inevitable in bulk studies of the loss tangent.

## VII. CONCLUSIONS

We successfully demonstrate the operation of a MET in which the bulk of the shunt capacitance is due to the junction itself. While not yet optimized for charge noise due to their rather low values of  $E_J/E_C$ , the devices still show reasonably good  $T_1$  and  $T_2$  values. Three devices each demonstrate a mean of  $T_1 > 80 \mu\text{s}$ , with instances of  $T_1$  exceeding  $100 \mu\text{s}$  for a period of hours. A simple scaling argument suggests that such good performance in a large-junction device implies that junction losses in small-junction devices are not the dominant limiting factor. Future work incorporating epitaxial dielectrics into a MET design could result in further improvement in performance, while also providing a possible pathway to greatly increase the areal density of superconducting qubits.

## ACKNOWLEDGMENTS

We thank the staff at the IBM Microelectronics Research Laboratory and Central Scientific Services for device fabrication. We also thank Oliver Dial for helpful discussions.

[1] J. Koch, T. M. Yu, J. Gambetta, A. A. Houck, D. I. Schuster, J. Majer, A. Blais, M. H. Devoret, S. M. Girvin, and R. J. Schoelkopf, Charge-insensitive qubit design derived from the Cooper pair box, *Phys. Rev. A* **76**, 042319 (2007).

- [2] P. Jurcevic, *et al.*, Demonstration of quantum volume 64 on a superconducting quantum computing system, *Quantum Sci. Technol.* **6**, 025020 (2021).
- [3] I. Aleiner, *et al.*, Accurately computing electronic properties of materials using eigenenergies, *ArXiv:2012.00921* (2020).
- [4] Y.-P. Shim and C. Tahan, Superconducting-semiconductor quantum devices: From qubits to particle detectors, *IEEE J. Sel. Top. Quantum Electron.* **21**, 1 (2015).
- [5] R. Zhao, S. Park, T. Zhao, M. Bal, C. R. H. McRae, J. Long, and D. P. Pappas, Merged-Element Transmon, *Phys. Rev. Appl.* **14**, 064006 (2020).
- [6] S. Oh, K. Cicak, J. S. Kline, M. A. Sillanpää, K. D. Osborn, J. D. Whittaker, R. W. Simmonds, and D. P. Pappas, Elimination of two level fluctuators in superconducting quantum bits by an epitaxial tunnel barrier, *Phys. Rev. B* **74**, 100502 (2006).
- [7] Y. Nakamura, H. Terai, K. Inomata, T. Yamamoto, W. Qiu, and Z. Wang, Superconducting qubits consisting of epitaxially grown NbN/AlN/NbN Josephson junctions, *Appl. Phys. Lett.* **99**, 212502 (2011).
- [8] J. M. Gambetta, C. E. Murray, Y.-K.-K. Fung, D. T. McClure, O. Dial, W. Shanks, J. W. Sleight, and M. Steffen, Investigating surface loss effects in superconducting transmon qubits, *IEEE Trans. Appl. Supercond.* **27**, 1 (2017).
- [9] J. M. Martinis, S. Nam, J. Aumentado, and C. Urbina, Rabi Oscillations in a Large Josephson-Junction Qubit, *Phys. Rev. Lett.* **89**, 117901 (2002).
- [10] J. M. Martinis, K. B. Cooper, R. McDermott, M. Steffen, M. Ansmann, K. D. Osborn, K. Cicak, S. Oh, D. P. Pappas, R. W. Simmonds, and C. C. Yu, Decoherence in Josephson Qubits from Dielectric Loss, *Phys. Rev. Lett.* **95**, 210503 (2005).
- [11] J. B. Hertzberg, E. J. Zhang, S. Rosenblatt, E. Magesan, J. A. Smolin, J.-B. Yau, V. P. Adiga, M. Sandberg, M. Brink, J. M. Chow, *et al.*, Laser-annealing Josephson junctions for yielding scaled-up superconducting quantum processors, *ArXiv:2009.00781* (2020).
- [12] A. P. M. Place, *et al.*, New material platform for superconducting transmon qubits with coherence times exceeding 0.3 milliseconds, *Nat. Commun.* **12**, 1779 (2021).
- [13] A. D. Córcoles, E. Magesan, S. J. Srinivasan, A. W. Cross, M. Steffen, J. M. Gambetta, and J. M. Chow, Demonstration of a quantum error detection code using a square lattice of four superconducting qubits, *Nat. Commun.* **6**, 6979 (2015).
- [14] J. M. Kreikebaum, K. P. O'Brien, A. Morvan, and I. Siddiqi, Improving wafer-scale Josephson junction resistance variation in superconducting quantum coherent circuits, *Supercond. Sci. Technol.* **33**, 06LT02 (2020).
- [15] M. V. Costache, G. Bridoux, I. Neumann, and S. O. Valenzuela, Lateral metallic devices made by a multiangle shadow evaporation technique, *J. Vac. Sci. Technol. B* **30**, 04E105 (2012).
- [16] A. Potts, G. J. Parker, J. J. Baumberg, and P. A. J. de Groot, CMOS compatible fabrication methods for sub-micron Josephson junction qubits, *IEE Proc.—Sci. Meas. Technol.* **148**, 225 (2001).
- [17] K. Zhang, M.-M. Li, Q. Liu, H.-F. Yu, and Y. Yu, Bridge-free fabrication process for Al/AlO<sub>x</sub>/Al Josephson junctions, *Chin. Phys. B* **26**, 78501 (2017).

- [18] H. Scherer, Th. Weimann, A. B. Zorin, and J. Niemeyer, The effect of thermal annealing on the properties of Al-AlOx-Al single electron tunneling transistors, *J. Appl. Phys.* **90**, 2528 (2001).
- [19] P. J. Koppinen, L. M. Väistö, and I. J. Maasilta, Complete stabilization and improvement of the characteristics of tunnel junctions by thermal annealing, *Appl. Phys. Lett.* **90**, 053503 (2007).
- [20] J. K. Julin, P. J. Koppinen, and I. J. Maasilta, Reduction of low-frequency  $1/f$  noise in Al-AlOx-Al tunnel junctions by thermal annealing, *Appl. Phys. Lett.* **97**, 152501 (2010).
- [21] I. M. Pop, T. Fournier, T. Crozes, F. Lecocq, I. Matei, B. Pannetier, O. Buisson, and W. Guichard, Fabrication of stable and reproducible submicron tunnel junctions, *J. Vac. Sci. Technol. B, Nanotechnol. Microelectron.: Mater. Proc. Meas. Phenom.* **30**, 010607 (2012).
- [22] The I-V measurement setup is similar to that described by M. Kjaergaard, *Proximity Induced Superconducting Properties in One and Two Dimensional Semiconductors*, Ph.D. thesis, Faculty of Science, Copenhagen University (2015). See Figure 3.11.
- [23] M. Tinkham, *Introduction to Superconductivity* (Courier Corporation, Mineola NY, 2004).
- [24] M. A. Gubrud, M. Ejrnaes, A. J. Berkley, R. C. Ramos, I. Jin, J. R. Anderson, A. J. Dragt, C. J. Lobb, and F. C. Wellstood, Sub-gap leakage in Nb/AlOx/Nb and Al/AlOx/Al Josephson junctions, *IEEE Trans. Appl. Supercond.* **11**, 1002 (2001).
- [25] See the Supplemental Material at <http://link.aps.org/supplemental/10.1103/PhysRevApplied.16.024023> for a description of the qubit measurement setup.
- [26] The main emphasis of our study is the  $T_1$  performance. Not all qubits are measured for  $T_2$  echo.
- [27] P. V. Klimov, *et al.*, Fluctuations of Energy-Relaxation Times in Superconducting Qubits, *Phys. Rev. Lett.* **121**, 090502 (2018).
- [28] K. B. Cooper, M. Steffen, R. McDermott, R. W. Simmonds, S. Oh, D. A. Hite, D. P. Pappas, and J. M. Martinis, Observation of Quantum Oscillations Between a Josephson Phase Qubit and a Microscopic Resonator using Fast Readout, *Phys. Rev. Lett.* **93**, 180401 (2004).
- [29] D. Gunnarsson, J.-M. Pirkkalainen, J. Li, G. Paraoanu, P. Hakonen, M. Sillanpää, and M. Prunnila, Dielectric losses in multi-layer Josephson junction qubits, *Supercond. Sci. Technol.* **26**, 085010 (2013).
- [30] Each of the six tunable devices has a total junction area of  $2.9 \mu\text{m}^2$  and an average measured frequency range of 1 GHz. The possible effect of the parasitic junction in the tunable devices is not taken into account.
- [31] J. Lisenfeld, A. Bilmes, A. Megrant, R. Barends, J. Kelly, P. Klimov, G. Weiss, J. M. Martinis, and A. V. Ustinov, Electric field spectroscopy of material defects in transmon qubits, *npj Quantum Inf.* **5**, 105 (2019).
- [32] C. Wang, C. Axline, Y. Y. Gao, T. Brecht, Y. Chu, L. Frunzio, M. H. Devoret, and R. J. Schoelkopf, Surface participation and dielectric loss in superconducting qubits, *Appl. Phys. Lett.* **107**, 162601 (2015).
- [33] D. P. Pappas, M. R. Vissers, D. S. Wisbey, J. S. Kline, and J. Gao, Two level system loss in superconducting microwave resonators, *IEEE Trans. Appl. Supercond.* **21**, 871 (2011).
- [34] C. Deng, M. Otto, and A. Lupascu, Characterization of low-temperature microwave loss of thin aluminum oxide formed by plasma oxidation, *Appl. Phys. Lett.* **104**, 043506 (2014).
- [35] Z. Kim, B. Suri, V. Zaretsky, S. Novikov, K. D. Osborn, A. Mizel, F. C. Wellstood, and B. S. Palmer, Decoupling a Cooper-Pair Box to Enhance the Lifetime to 0.2 ms, *Phys. Rev. Lett.* **106**, 120501 (2011).